



Report

Computational Finance

Lab Assignment #2

Sunday 11th May, 2025 20:40

Student(s):

Maarten Stork (15761770)
Lucas Keijzer (14041073)
Pemmasani Prabakaran Rohith Saai (14968061)

Details:

Lecturer: Sven Karbach
Course: Computational Finance
Course Code: 5284COFI6Y

1 Introduction

Monte Carlo methods have long been a cornerstone of quantitative finance, beginning with Boyle's 1977 application of simulation to option pricing (Boyle, 1977). By sampling asset-price paths from a chosen stochastic model, Monte Carlo (MC) simulation approximates expected payoffs—converging to theoretical values by the law of large numbers. This approach is especially important for complex or path-dependent securities where closed-form solutions are unavailable. Although plain Monte Carlo can converge slowly, variance-reduction techniques can greatly improve efficiency. In this report, we first establish an analytic foundation for variance swaps, then move on to Monte Carlo applications in Asian options and weather derivatives.

The first part delivers a closed-form treatment of variance swaps. We derive the continuous-time payoff identity, show how a static portfolio of log-contracts plus the underlying replicates realized variance, and compute the fair swap strike under Heston's stochastic volatility via an ODE. This analytic exercise shows how realized variance can be replicated—and therefore traded—using a static portfolio of log-contracts and the underlying asset.

Having seen how variance swaps admit analytic solutions, we then confront derivatives that resist such formulas, tackling arithmetic Asian options under the Heston model. These path-dependent payoffs lack closed-form values, so here we actually need to employ Monte Carlo simulation to get reliable results. To accelerate convergence, we introduce control variates—using the known price of a geometric Asian option to cut variance in estimating the arithmetic payoff. This illustrates how variance-reduction transforms raw simulation into a practical pricing tool for stochastic-volatility models.

Finally, we extend MC methods to temperature-based weather derivatives, where payouts depend on

cumulative temperature indices (e.g. heating degree days). Here, analytic pricing is typically intractable, so we model temperature as a seasonal, mean-reverting process calibrated to historical data, simulate numerous weather paths, and compute expected payouts. This section demonstrates Monte Carlo's versatility in capturing uncertainty beyond traditional financial assets—underscoring its role in both theory and real-world risk management.

Together, these three parts showcase different quantitative techniques—from exact analytic formulas to simulation with variance reduction—that share a common goal: modelling a coherent framework for modern derivative pricing. We also show at what point such a computational-heavy approach becomes necessary and how this gives us results we can actually build on. This report is structured into three sections, each corresponding to one of these sub-areas and additionally to one of the assigned tasks for the Computational Finance course at the University of Amsterdam. Each section includes its own methods, results, and discussion, while on top of that the paper as a whole features a unified introduction and conclusion. For full implementation details, see the complete code on GitHub ¹.

2 Realized Variance Swap

2.1 Introduction

Understanding and accurately pricing variance swaps is essential for managing volatility risk in financial markets. These derivatives allow investors to trade future realized volatility against implied levels, offering a pure exposure to market uncertainty without directional risk. In this section, we explore the theoretical pricing and hedging of realized variance swaps under stochastic volatility models, particularly the Heston model, and analyze their decomposition into more tractable financial instruments such as log contracts. The results provide insight into how option markets reflect and manage expectations of market variance.

2.2 Methods

We first develop a fully analytical approach to pricing realized variance swaps. We begin by expressing the accumulated variance as a function of the asset's price path, using Itô calculus to derive a payoff identity involving log returns and stochastic integrals. This identity allows the variance swap to be represented in terms of a log contract and a dynamic position in the underlying asset.

Using risk-neutral valuation, we decompose the swap's value into three components: the price of a log contract, the gain from holding the underlying, and a deterministic cash term. We then construct a hedging portfolio replicating the swap payoff, and verify that it is self-financing.

Finally, under the Heston stochastic volatility model, we compute the expected realized variance by solving a linear ODE for the variance process. This yields a closed-form expression for the fair variance swap rate. As this section focuses on instruments admitting exact valuation, all results are derived analytically without simulation.

2.3 Results

These results differ slightly from those in the subsequent overarching sections, as they are not based on (MC-)experiments but derived from exact calculations. Nonetheless, this is the most appropriate place in

¹See source code and documentation at: https://github.com/Lucas-Keijzer/CompFinance_ass_1

the report to present them. The subsections (2.3.1, 2.3.2, ...) correspond to the distinct sections defined in the original assignment.

2.3.1 Itô's formula

We wish to show

$$\int_0^T \sigma_t^2 dt = 2 \int_0^T \frac{dS_t}{S_t} - 2 \log\left(\frac{S_T}{S_0}\right). \quad (1)$$

To prove this, we apply Itô's formula to $f(x) = \log x$ and the SDE

$$dS_t = rS_t dt + \sigma_t S_t dB_t. \quad (2)$$

Recall

$$d(\log S_t) = f'(S_t) dS_t + \frac{1}{2} f''(S_t) (dS_t)^2, \quad f'(x) = \frac{1}{x}, \quad f''(x) = -\frac{1}{x^2}.$$

Since $(dS_t)^2 = \sigma_t^2 S_t^2 dt$, we get

$$\begin{aligned} d \log S_t &= \frac{1}{S_t} (rS_t dt + \sigma_t S_t dB_t) - \frac{1}{2} \frac{1}{S_t^2} (\sigma_t^2 S_t^2 dt) \\ &= \left(r - \frac{1}{2} \sigma_t^2\right) dt + \sigma_t dB_t. \end{aligned}$$

Rearrange to isolate $\sigma_t^2 dt$:

$$\sigma_t^2 dt = 2(d \log S_t - r dt) = 2 \frac{dS_t}{S_t} - 2 d \log S_t,$$

where we used $dS_t/S_t = r dt + \sigma_t dB_t$. Integrate from 0 to T :

$$\int_0^T \sigma_t^2 dt = 2 \int_0^T \frac{dS_t}{S_t} - 2 \int_0^T d \log S_t.$$

Finally, since $\int_0^T d \log S_t = \log S_T - \log S_0 = \log\left(\frac{S_T}{S_0}\right)$, we obtain

$$\int_0^T \sigma_t^2 dt = 2 \int_0^T \frac{dS_t}{S_t} - 2 \log\left(\frac{S_T}{S_0}\right),$$

which indeed recovers the identity stated in (1).

2.3.2 Variance-Swap Decomposition

Starting from,

$$V_t = e^{-r(T-t)} \mathbb{E}_Q \left[\int_0^T \sigma_t^2 dt \mid \mathcal{F}_t \right]. \quad (3)$$

Substitute the identity:

$$\int_0^T \sigma_t^2 dt = 2 \int_0^T \frac{dS_t}{S_t} - 2 \log\left(\frac{S_T}{S_0}\right). \quad (4)$$

to obtain

$$V_t = 2e^{-r(T-t)} \mathbb{E}_Q \left[\int_0^T \frac{dS_t}{S_t} \mid \mathcal{F}_t \right] - 2e^{-r(T-t)} \mathbb{E}_Q \left[\log\left(\frac{S_T}{S_0}\right) \mid \mathcal{F}_t \right].$$

Split the first expectation at t and use $\mathbb{E}_Q[dS_s/S_s \mid \mathcal{F}_t] = r ds$ for $s \geq t$:

$$\mathbb{E}_Q \left[\int_0^T \frac{dS_u}{S_u} \mid \mathcal{F}_t \right] = \int_0^t \frac{dS_u}{S_u} + \mathbb{E}_Q \left[\int_t^T \frac{dS_u}{S_u} \mid \mathcal{F}_t \right] = \int_0^t \frac{dS_u}{S_u} + r(T-t).$$

Now introduce L_t as

$$L_t := -2e^{-r(T-t)} \mathbb{E}_Q \left[\log\left(\frac{S_T}{S_0}\right) \mid \mathcal{F}_t \right]. \quad (5)$$

Putting these pieces together yields exactly the decomposition

$$V_t = L_t + 2r(T-t)e^{-r(T-t)} + 2e^{-r(T-t)} \int_0^t \frac{dS_u}{S_u}. \quad (6)$$

2.3.3 Hedging the realized-variance swap

We build the portfolio

$$\Pi_t = L_t + \phi_t S_t + \psi_t A_t, \quad (7)$$

where $A_t = e^{rt}$ and the trading weights are

$$\phi_t = \frac{2e^{-r(T-t)}}{S_t}, \quad \psi_t = 2e^{-rt} \left(\int_0^t \frac{dS_u}{S_u} + (T-t)r - 1 \right). \quad (8)$$

For the replication of V_t , starting from $\Pi_t = L_t + \phi_t S_t + \psi_t A_t$, we plug in (8) and simplify term by term:

$$\phi_t S_t = 2e^{-r(T-t)},$$

$$\psi_t A_t = 2e^{-rt} \left(\int_0^t \frac{dS_u}{S_u} + (T-t)r - 1 \right) e^{rt} = 2 \left(\int_0^t \frac{dS_u}{S_u} + (T-t)r - 1 \right).$$

Hence

$$\Pi_t = L_t + 2e^{-r(T-t)} + 2 \left(\int_0^t \frac{dS_u}{S_u} + (T-t)r - 1 \right).$$

Combine constants:

$$2e^{-r(T-t)} - 2 = -2(1 - e^{-r(T-t)}) = 2r(T-t)e^{-r(T-t)},$$

so overall

$$V_t = L_t + 2r(T-t)e^{-r(T-t)} + 2e^{-r(T-t)} \int_0^t \frac{dS_u}{S_u}. \quad (9)$$

which by (6) is exactly V_t .

Next, to show potential self-financing property, a portfolio $\Pi_t = \phi_t S_t + \psi_t A_t$ (together with a position in L_t) is self-financing if

$$d\Pi_t = \phi_t dS_t + \psi_t dA_t,$$

i.e. all changes in value come from gains and losses on the holdings, with no external cash flows.

Starting from $\Pi_t = L_t + \phi_t S_t + \psi_t A_t$, apply Itô's product rule:

$$d(L_t) + d(\phi_t S_t) + d(\psi_t A_t) = dL_t + \phi_t dS_t + S_t d\phi_t + \psi_t dA_t + A_t d\psi_t.$$

By construction of ϕ_t and ψ_t in (8), one checks that

$$S_t d\phi_t + A_t d\psi_t = 0.$$

Hence

$$d\Pi_t = dL_t + \phi_t dS_t + \psi_t dA_t.$$

But from the decomposition of dV_t (see part 2), we know $dV_t = dL_t + \phi_t dS_t + \psi_t dA_t$. It follows that

$$d\Pi_t = dV_t \implies \Pi_t = V_t, \forall t,$$

and since $d\Pi_t$ involved only $\phi_t dS_t$ and $\psi_t dA_t$, the portfolio is self-financing.

2.3.4 Expected realized variance under the Heston model

Consider the variance-process dynamics

$$dV_t = \kappa(\theta - V_t) dt + \sigma\sqrt{V_t} dW_t, \quad V_0 \text{ given.} \quad (10)$$

We wish to compute the time-average $\frac{1}{T} \mathbb{E}[\int_0^T V_t dt]$. To this end, define the mean function

$$u(t) := \mathbb{E}[V_t].$$

Since $V_t \geq 0$ and has finite expectation, Fubini's theorem allows us to swap expectation and integration:

$$\frac{1}{T} \mathbb{E}\left[\int_0^T V_t dt\right] = \frac{1}{T} \int_0^T \mathbb{E}[V_t] dt = \frac{1}{T} \int_0^T u(t) dt. \quad (11)$$

Next, integrate the SDE (10) from 0 to t ,

$$V_t - V_0 = \kappa \int_0^t (\theta - V_s) ds + \sigma \int_0^t \sqrt{V_s} dW_s.$$

Taking expectations and using the fact that the Itô integral has zero mean yields

$$u(t) - V_0 = \kappa \int_0^t (\theta - u(s)) ds.$$

Differentiating in t gives the linear ODE

$$u'(t) = \kappa(\theta - u(t)), \quad u(0) = V_0. \quad (12)$$

The standard integrating-factor method (multiply by $e^{\kappa t}$ and integrate) shows that

$$u(t) = \theta + (V_0 - \theta)e^{-\kappa t}. \quad (13)$$

Finally, substitute (13) into the explicit $u(t)$:

$$\int_0^T u(t) dt = \int_0^T \left[\theta + (V_0 - \theta)e^{-\kappa t} \right] dt = \theta T + \frac{V_0 - \theta}{\kappa} (1 - e^{-\kappa T}),$$

so that

$$\frac{1}{T} \mathbb{E} \left[\int_0^T V_t dt \right] = \theta + \frac{V_0 - \theta}{\kappa T} (1 - e^{-\kappa T}). \quad (14)$$

2.3.5 Variance swap rate under the Heston-type model

We begin with the definition of the variance swap rate:

$$V_{ST} := \frac{1}{T} \mathbb{E} \left[\lim_{N \rightarrow \infty} \sum_{k=1}^N \left(\frac{S_{kT/N} - S_{(k-1)T/N}}{S_{(k-1)T/N}} \right)^2 \right] = \frac{1}{T} \mathbb{E} \left[\int_0^T \frac{1}{S_t^2} (dS_t)^2 \right]. \quad (15)$$

Under the Heston-type dynamics

$$\begin{cases} dS_t = (r - \alpha V_t) S_t dt + S_t \sqrt{\beta + V_t} dB_t, \\ dV_t = \kappa(\theta - V_t) dt + \sigma \sqrt{V_t} dW_t, \end{cases} \quad (16)$$

with $\langle B, W \rangle_t = \rho t$, the quadratic variation term is

$$(dS_t)^2 = S_t^2 (\beta + V_t) dt \implies \frac{1}{S_t^2} (dS_t)^2 = (\beta + V_t) dt. \quad (17)$$

Substituting (17) into (15) gives

$$V_{ST} = \frac{1}{T} \mathbb{E} \left[\int_0^T (\beta + V_t) dt \right] = \beta + \frac{1}{T} \int_0^T \mathbb{E}[V_t] dt. \quad (18)$$

But $\mathbb{E}[V_t] = u(t)$ was found in (13):

$$u(t) = \theta + (V_0 - \theta)e^{-\kappa t} \implies \int_0^T u(t) dt = \theta T + \frac{V_0 - \theta}{\kappa} (1 - e^{-\kappa T}).$$

Hence the closed-form expression is

$$V_{ST} = \beta + \frac{1}{T} \left[\theta T + \frac{V_0 - \theta}{\kappa} (1 - e^{-\kappa T}) \right] = \beta + \theta + \frac{V_0 - \theta}{\kappa T} (1 - e^{-\kappa T}). \quad (19)$$

Note: The correlation ρ enters only the joint fluctuations of B_t and W_t , but when we take expectations the stochastic term in the V_t SDE drops out. Concretely,

$$\frac{d}{dt}[V_t] = \kappa(\theta - [V_t]), \quad [V_0] = V_0,$$

which is a deterministic ODE independent of ρ . Hence ρ plays no role in the expression for V_{ST} in (18).

2.4 Discussion & Concluding Remarks

The Itô-derived identity reduces the path-dependent realized variance payoff to observable log-return terms, enabling its expression through standard instruments. By decomposing the swap price into a log-contract, a dynamically maintained position in the underlying, and a deterministic cash adjustment, we obtain a

replication strategy that is both practical and self-financing. This confirms that realized variance swaps can be perfectly hedged in continuous markets, validating their no-arbitrage pricing.

Under the Heston model, the closed-form expected variance highlights the roles of the initial variance and mean-reversion speed: rapid reversion anchors realized variance around its long-term mean, whereas slow reversion prolongs the influence of the starting level. Overall, these analytic results furnish both a precise pricing benchmark and insight into how variance dynamics shape swap strikes.

3 Variance Reduction: Asian Options under the Heston Model

3.1 Introduction

While Monte-Carlo methods are paramount to quantitative finance, convergence rate of the method diminishes at the rate of $\frac{1}{\sqrt{N}}$, where N is the number of samples of a 1-D random variable. For higher-dimensional random variables, the convergence rate further worsens as it scales at a rate of $(\frac{1}{N})^k$. This degradation in performance due to increasing dimensionality is often referred to as the *curse of dimensionality*, thus posing significant computational constraints. As a result, several variance reduction strategies have been explored to improve the convergence rate, which includes antithetic variates and a more advanced approach—employed here—is the control variates. To reduce the variance of a random variable X with control variates, we introduce another random variable Y whose expectation ($\mathbb{E}[Y] = \mu$) is known (in our case, analytically). The adjusted estimator becomes (Hull & White, 1988)

$$\tilde{X} = \mathbb{E}[X + c(Y - \mu)]. \quad (20)$$

Its variance is

$$\text{Var}[X + c(Y - \mu)] = \text{Var}[X] + c^2 \text{Var}[Y] + 2c \text{Cov}[X, Y].$$

Choosing

$$c = -\frac{\text{Cov}[X, Y]}{\text{Var}[Y]}$$

minimises this expression, yielding

$$\text{Var}[X + c(Y - \mu)] = \text{Var}[X] - \frac{\text{Cov}[X, Y]^2}{\text{Var}[Y]},$$

so a high correlation between X and Y effectively reduces the variance of the estimator.

In this section, we evaluate the efficacy of control variate variance reduction strategy for pricing Asian options under the Heston Model. For an underlying asset $(S_t)_{t \in [0, T]}$, the price of an Asian call option C is given by

$$C = \max \left(\frac{1}{T} \int_0^T S_t - K, 0 \right) \quad (21)$$

where,

K is the strike price

S_t is the underlying price

T is the maturity period

For modeling of the price of an Asian call option defined on the underlying asset S_t , a discretized Heston model is used. In contrast to the Black-Scholes model where the implied volatility σ_{imp} is assumed to be constant, the Heston model defines the volatility of the asset as a stochastic process, removing the dependency of the implied volatility on the strike price K and maturity period T under the Black-Scholes model. For the purpose of variance reduction, we simulate the price of the underlying asset S_t using the Euler and Milstein schemes. Under the Euler geometric scheme, the price of the underlying asset at time $S_{t+\Delta t}$ is given by

$$\hat{S}_{t+\Delta t} = \hat{S}_t \exp((r - \frac{1}{2}\hat{V}_t^+)\Delta t + \sqrt{\hat{V}_t^+\Delta t} Z_S) \quad (22)$$

where, the variance $\hat{V}_{t+\Delta t}$ is given by

$$\hat{V}_{t+\Delta t} = \hat{V}_t + \kappa(\theta - \hat{V}_t^+)\Delta t + \xi\sqrt{\hat{V}_t^+\Delta t} Z_V \quad (23)$$

Under the Milstein geometric method, the price of the underlying asset at time $S_{t+\Delta t}$ is given by:

$$\hat{S}_{t+\Delta t} = \hat{S}_t \exp((r - \frac{1}{2}\hat{V}_t^+)\Delta t + \sqrt{\hat{V}_t^+\Delta t} Z_S) \quad (24)$$

where, the variance $\hat{V}_{t+\Delta t}$ is given by

$$\hat{V}_{t+\Delta t} = \hat{V}_t + \kappa(\theta - \hat{V}_t^+)\Delta t + \xi\sqrt{\hat{V}_t^+\Delta t} Z_V + \frac{1}{4}\xi^2\Delta t(Z_V^2 - 1) \quad (25)$$

where,

\hat{S}_t is the underlying price at time t

Δt is the time step

r is the risk-free rate

κ is the mean reversion coefficient

θ is the long-term mean of variance

ξ is the volatility-of-volatility

$Z_V = Z_1$ is a standard normal variable

Z_2 is a standard normal variable

$Z_S = \rho Z_1 + \sqrt{1 - \rho^2} Z_2$ is a correlated normal variable

ρ is correlation

For the purpose of variance reduction, the control variate X in 20 is defined as the price of an Asian call

option modeled under the geometric Brownian motion model. Under the Euler discretization model of the Black-Scholes model, the price of the underlying S_t is defined as

$$\hat{S}_{t+\Delta t} = \hat{S}_t + r\hat{S}_t\Delta t + \sigma\hat{S}_t\sqrt{\Delta t}Z \quad (26)$$

where,

σ is volatility

Z is a standard normal variable

3.2 Methods

To simulate the paths of the underlying model using the Heston Model, we assume the following parameters in Table 1:

Parameter	Value
Initial asset price S_0	100
Initial variance V_0	0.04
Risk-free rate r	0.06
Mean reversion speed κ	2.0
Long-run variance θ	0.04
Volatility of volatility ξ	0.25
Correlation ρ	-0.9
Time to maturity T	1.0
Strike price K	100
Time steps N	1000
Simulated paths M	10,000

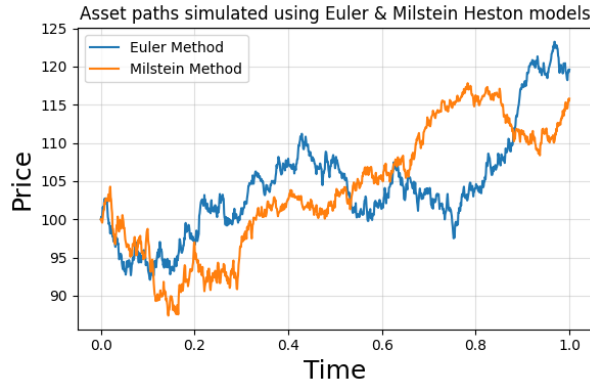
Table 1: Model Parameters for Heston Simulation

For the Euler and Milstein schemes, we use the geometric model for the underlying asset. Using these simulated values, we calculate the Asian asset price. For experimenting the impact of the number of paths and sensitivity analysis, we vary $M = [100, 1000, 10,000, 100,000]$, $\rho = [-0.9, 0.5]$ with increments of 0.1, $\xi = [0.1, 1.0]$ with increments of 0.1 and $\kappa = [90, 95, 100, 105, 110]$. For these experiments, we hold the all constant similar to the base setting while only changing one parameter at a time. Implementation were done in Python using the Numpy library and plots were created using the Matplotlib library.

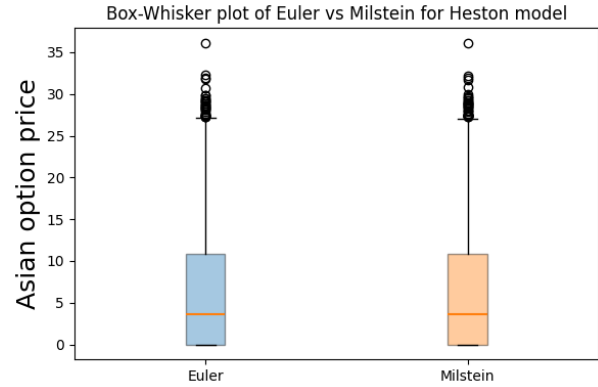
3.3 Results

3.3.1 Monte Carlo Simulation under Heston Model

Using the Euler and Milstein discretization method of the Heston model, sample paths of the underlying assets were simulated, as illustrated in Figure 1a. Using these simulated samples, the arithmetic-average Asian call option prices were determined, with its median and spread depicted in Figure 1b. As seen in Table 2, the prices and standard error (95% CI) of the Asian call option are tabulated. To compare the Euler and Milstein scheme for Heston model, strong and weak convergence tests were performed. From Figure 2, we can infer that both schemes converged exactly as theory predicts for a Heston model. Euler scheme exhibited

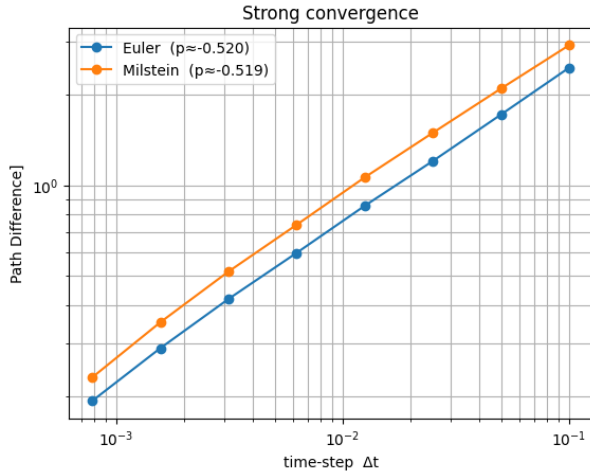


(a) Asset paths simulated with Euler and Milstein schemes.

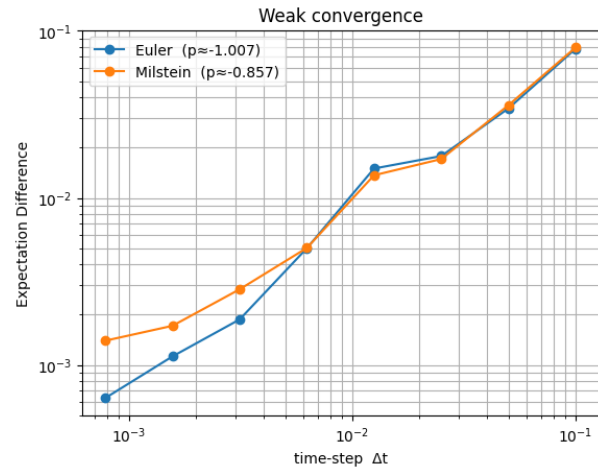


(b) Box-whisker plot of Asian call prices under Heston model

Figure 1: Monte-Carlo simulation results under the Heston model.



(a) Path-wise error (Strong convergence) for Euler and Milstein discretization scheme



(b) Price error (Weak convergence) for Euler and Milstein discretization scheme

Figure 2: Convergence of Euler and Milstein discretization scheme for Heston model

a rate of $\frac{1}{2}$ in the strong sense (path-wise error) and 1 in the weak sense (price error). However, Milstein scheme exhibited a rate of $\frac{1}{2}$ in the strong sense (path-wise error) as seen for Euler. In pricing terms (weak convergence) both methods land near order 1, and thus, for plain discretization, Milstein costs more per step yet delivers no tangible accuracy gain over Euler. Therefore, to improve performance of the Milstein scheme, we need to atleast double the number of samples or perform variance reduction.

Moreover, to benchmark these results, the volatility-of-volatility was set to zero ($\xi = 0$), thereby reducing the Heston model to Geometric Brownian Model (GBM), and compared with the results generated from a GBM model's Asian call option price. From these results, we can see that by setting the volatility-of-volatility $\xi = 0$, the Heston model reduces to a GBM where the volatility of the model is deterministic as evidenced by the small absolute difference in the estimated Asian call price between the Heston and GBM model in Table 3.

Method	Price \pm Std (95% C.I)
Heston Euler	6.0719 \pm 0.1343
Heston Milstein	6.0723 \pm 0.1343

Table 2: Asian call option prices simulated using Euler and Milstein discretization of the Heston Model

Model	Price \pm Std (95% C.I)	Absolute Difference
Heston Euler $\xi = 0$	6.0053 \pm 0.1581	0.0000
GBM Euler	6.0053 \pm 0.1581	
Heston Milstein $\xi = 0$	6.0056 \pm 0.1581	0.0003
GBM Milstein	6.0053 \pm 0.1581	

Table 3: Benchmarking results of the Heston model by setting $\xi = 0$

3.3.2 Analytical Geometric-Asian Price as Control Variate Reference

The geometric-average Asian call price under the Black-Scholes model is implemented using the following formulation:

$$C_G = S_0 e^{(\hat{r}-r)T} \Phi(d_1) - K e^{-rT} \Phi(d_2) \quad (27)$$

with,

$$d_1 = \frac{\log(\frac{S_0}{K}) + (\hat{r} + \frac{1}{2}\hat{\sigma}^2)T}{\sqrt{T}\hat{\sigma}} \quad (28)$$

$$d_2 = \frac{\log(\frac{S_0}{K}) + (\hat{r} - \frac{1}{2}\hat{\sigma}^2)T}{\sqrt{T}\hat{\sigma}} \quad (29)$$

$$\hat{\sigma} = \sigma \sqrt{\frac{2N+1}{6(N+1)}} \quad (30)$$

$$\hat{r} = \frac{(r - \frac{1}{2}\sigma^2) + \hat{\sigma}^2}{2} \quad (31)$$

Here, the implied volatility σ_{imp} is defined as

$$\sigma_{\text{imp}}(K, T) = \sqrt{\theta + \frac{(v_0 - \theta)(1 - e^{-KT})}{KT}} \quad (32)$$

From the implementation, the analytical Asian call price for the defined underlying under the specified

Method	Simulated Price	Analytical Price	Absolute Difference
Heston Euler $\xi = 0$	6.0053	5.7823	0.229
Heston Milstein $\xi = 0$	6.0056	5.7823	0.223

Table 4: Accuracy check of the Heston model by setting $\xi = 0$ and analytical geometric-average Asian call price

conditions is 5.7823. There is significant difference between the MC approximation and analytical value.

However, this can be explained by the number of paths sampled. To test this accuracy, we also calculate the absolute difference between the Monte-Carlo Asian call price derived from Euler and Milstein schemes of Heston model when $\xi = 0$ and the analytic price, as the Heston model reduces to a GBM under this condition as seen in Table 4

3.3.3 Implementing the Control Variate Monte Carlo

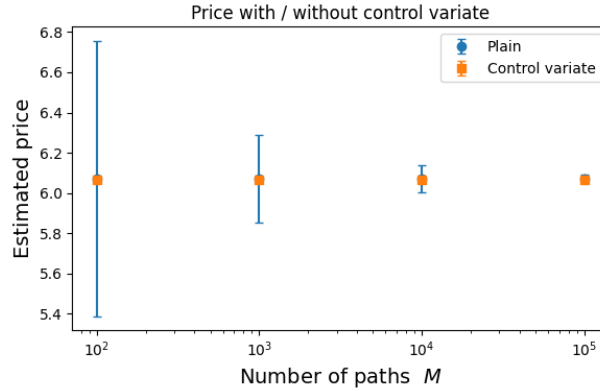
Under the defined settings and $c = 1$, we observe that the variance of the plain estimator of the Heston model under Euler discretization is 0.0047 with a standard error of 0.1343 in the 95% CI. Using the control variate method with the analytical geometric Asian call price as C_G , we observe that the variance of the control variate estimator of the Heston model under Euler discretization is 0.0004 with a standard error of 0.0410 in the 95% CI, resulting in a variance reduction of 10.7x reduction in variance.

Similarly, we observe that the variance of the plain estimator of the Heston model under Milstein discretization is 0.0047 with a standard error of 0.1343 in the 95% CI. Using the control variate method with the analytical geometric Asian call price as C_G , we observe that the variance of the control variate estimator of the Heston model under Milstein discretization is 0.0004 with a standard error of 0.0409 in the 95% CI, resulting in a variance reduction of 10.8x reduction in variance.

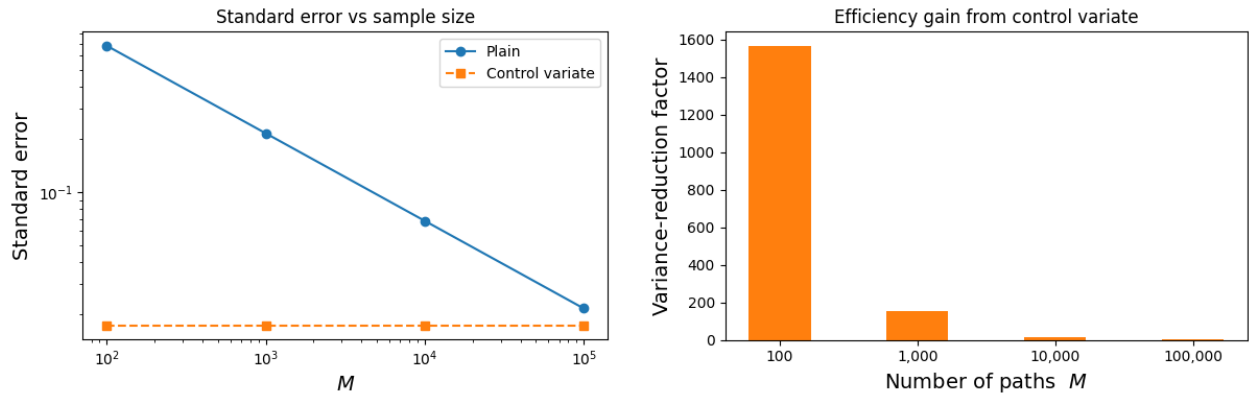
3.4 Experiments and Comparative Analysis

Firstly, we evaluate the performance of control variates by comparing the estimated prices and standard errors with and without control variates across various numbers of simulation paths. Here, the results are presented from the Milstein scheme as no significant difference in behaviour was observed with increased number between the two schemes. In Figure 3a, we can observe that as the increasing number of simulated path, the standard error decreases for the plain estimate thereby increasing the confidence in our prediction of the Asian call price. However, for the control variate estimates, even with low number of paths, the standard error remains low, exhibiting the superior performance of the control variate method. In Figure 3b and 3c, the reduction in standard error and efficiency gain with respect to variance reduction is further highlighted where we observe that the control variate method produces confident estimates of the Asian call prices even at with low number of samples, when compared to the plain estimate.

Secondly, we evaluate the impact of the correlation coefficient ρ in the generation of correlated normal variables. Here and in the following sections, we do not discuss about the standard error as they do not vary much and contribute to the discuss. They are however plotted in the Figure for completeness. In Figure 4, we observe that as ρ increases from -0.9 to 0.5 , the option price shows a clear decreasing trend. This behavior is intuitive under the Heston model: negative correlation tends to reduce volatility spikes when the asset price drops, stabilizing upward moves and supporting higher average prices, which benefit call options. Conversely, positive correlation enhances volatility during price drops, increasing the likelihood of lower average prices and thus reducing the option's value. Both the plain and control variate-adjusted prices are nearly indistinguishable, again demonstrating the accuracy and efficiency of the variance reduction technique.



(a) Estimated Asian call price for Milstein schemes of Heston model across different number of paths



(b) Standard error of the Euler and Milstein scheme of Heston model across different number of paths

(c) Variance reduction of the Euler and Milstein scheme of Heston model across different number of paths

Figure 3: Evaluation of the performance of control variates with and without control variates across various numbers of paths

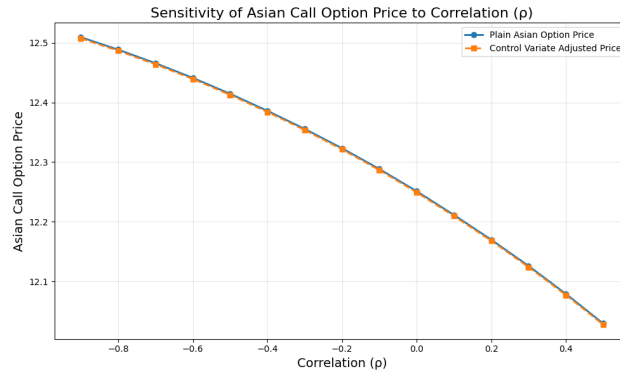


Figure 4: Estimated Asian call price for Euler and Milstein schemes of Heston model across different number of paths

Thirdly, we evaluate the impact of the volatility-of-volatility ξ on the price of the Asian call option price. In Figure 5, we observe that the option price initially increases slightly with low values of ξ , peaking around

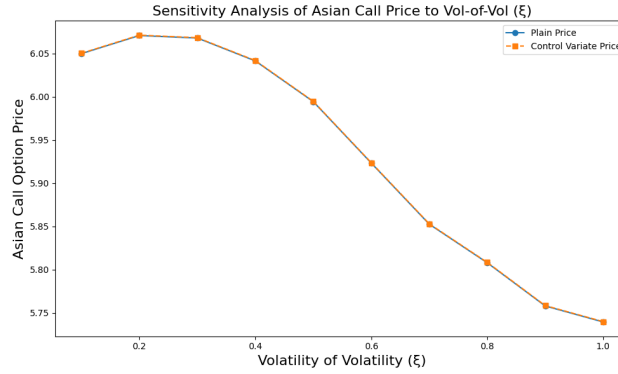


Figure 5: *Estimated Asian call price for Milstein schemes of Heston model across different values of ξ*

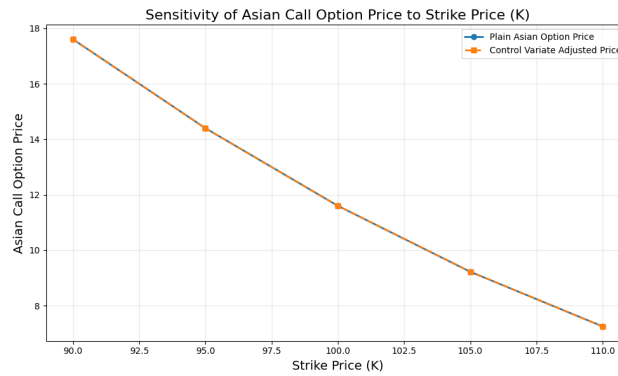


Figure 6: *Estimated Asian call price for Milstein schemes of Heston model across different values of K*

$\xi = 0.3$, after which it steadily declines as ξ continues to rise toward 1.0. Both the plain Monte Carlo price and the control variate-adjusted price closely follow the same trend, indicating a consistent relationship. The decreasing trend at higher volatility of volatility values suggests that increased uncertainty in volatility tends to slightly reduce the expected payoff of the Asian call option. Additionally, the closeness of the two curves indicates that the control variate method provides only a marginal improvement in variance reduction in this specific scenario.

Next, we evaluate the impact of the strike price K on the price of the Asian call option price. In Figure 6, we observe that the option price decreases steadily and almost linearly as the strike price increases from 90 to 110. This behavior aligns with financial intuition: higher strike prices make the option less likely to end up in-the-money, reducing its expected payoff. Both the plain Monte Carlo estimates and the control variate-adjusted prices closely follow each other, confirming the robustness of the control variate technique without introducing bias. This also suggests that strike price is a dominant factor influencing option value, with strong inverse sensitivity.

Finally, we estimate the optimal control variate coefficient c^* which is defined as $c^* = \frac{Cov(X,Y)}{Var(Y)}$. Using this optimal value, we observe that the variance of the plain estimator of the Heston model under Milstein discretization is 0.0047 with a standard error of 0.1343 in the 95% CI. Using the control variate method with the analytical geometric Asian call price as C_G , we observe that the variance of the control variate estimator of the Heston model under Euler discretization is 0.0003 with a standard error of 0.0339 in the 95% CI, resulting in a variance reduction of 15.6x reduction in variance.

3.5 Conclusion

In this section, we demonstrate the effectiveness of the control variate technique in reducing the variance of Monte Carlo estimators for Asian call option pricing under the Heston stochastic volatility model using Euler and Milstein discretization schemes. By leveraging the analytical geometric-average Asian option price as a control variate, we achieve a substantial reduction in variance—over 10x using a simple coefficient and up to 15.6x with the optimal coefficient—without introducing bias to the estimator. Sensitivity analyses across key parameters such as the correlation coefficient ρ , volatility-of-volatility ξ , and strike price K further confirm the model's robustness and the consistent performance of the variance reduction method. The results highlight intuitive relationships: option prices decrease with higher strike prices and positive correlation, while increased volatility-of-volatility initially raises then dampens option value. Overall, the control variate method significantly improves estimator efficiency, enabling more accurate pricing with fewer simulations, making it a valuable tool in computational finance applications involving high-dimensional or complex stochastic models like Heston.

4 The Temperature Derivative Market — Pricing of Asian Temperature Risk

4.1 Introduction

Weather derivatives are financial instruments used to hedge risks associated with weather variability. They typically base payoffs on observable weather indices (e.g. temperature) rather than on actual losses. A common underlying parameter is the average daily temperature, defined as

$$T_t = \frac{T_t^{\max} + T_t^{\min}}{2}, \quad (33)$$

and contracts are often written on cumulative indices such as Heating Degree Days (HDD) or Cooling Degree Days (CDD), with it being important to note the Cumulative Average Temperature (CAT), all defined as follows:

$$\text{HDD}(\tau_1, \tau_2) = \int_{\tau_1}^{\tau_2} \max(c - T_u, 0) du, \quad (34)$$

$$\text{CDD}(\tau_1, \tau_2) = \int_{\tau_1}^{\tau_2} \max(T_u - c, 0) du, \quad (35)$$

$$\text{CAT}(\tau_1, \tau_2) = \int_{\tau_1}^{\tau_2} T_u du, \quad (36)$$

where c is a reference temperature (typically 18°C). For instance, gas and power companies often use HDD or CDD contracts to smooth earnings against seasonal demand fluctuations. Industries such as energy, agriculture, retail, tourism, and finance commonly utilize weather derivatives for risk management: energy companies hedge revenue against mild winters or warm summers (consumption shifts), tourism-companies mitigate seasonal sales variability due to weather changes and financial institutions include weather derivatives in broader risk portfolios. This report constructs and calibrates a stochastic temperature model for Amsterdam and uses it to price short-term HDD option contracts. This is useful for quantifying weather-related financial risk and informing decision-making in (energy) markets, and further gives us new insights

for our overarching Monte Carlo-related report.

4.2 Methods

Data Source and Preprocessing: We collected historical daily average temperature data (2-meter air temperature) for Amsterdam over a recent multi-year period (2020-2024), obtained from the `Open-Meteo` package². This produced a time series T_t of daily average temperatures, which serves as the underlying meteorological parameter in our model calibration. All analysis and model calibration are conducted under the real-world probability measure P using this daily temperature time series. Prior to analysis, we implemented a robust preprocessing pipeline to handle missing values through time-based interpolation, which preserves the temporal structure of the data while ensuring completeness of the series.

Deterministic Seasonal Model: We express the daily temperature as $T_t = \bar{\mu}(t) + r_t$, where $\bar{\mu}(t)$ is the deterministic seasonal mean and r_t is the stochastic residual. The function $\bar{\mu}(t)$ captures the long-term trend and annual seasonality in temperatures. We model it as a linear trend plus a sinusoidal cycle with a one-year period:

$$\bar{\mu}(t) = a + bt + \alpha \sin\left(\frac{2\pi}{365.25}t + \theta\right) \quad (37)$$

where a represents the baseline temperature, b captures the linear trend (potentially reflecting climate change effects), α is the amplitude of seasonal oscillations, and θ is the phase shift. The parameters of this seasonal mean model are estimated via non-linear least-squares regression using the `scipy.optimize.curve_fit` function³, ensuring that $\bar{\mu}(t)$ closely approximates the observed seasonal pattern (so that $\mathbb{E}[T_t] \approx \bar{\mu}(t)$).

AR Modeling of Residuals: After removing the seasonal mean, the remaining residual series $r_t = T_t - \bar{\mu}(t)$ represents short-term temperature fluctuations around zero. We model r_t as an autoregressive process of order p , $\text{AR}(p)$, to capture the serial correlation and mean-reverting behavior in these daily anomalies. The model order p is selected using information criteria, in our case we use Akaike Information Criterion (AIC) and Bayesian Information Criterion (BIC). In our case BIC suggests a more parsimonious model, while AIC favors a more complex model. To find a good balance we use the elbow method, where we find that $\text{AR}(7)$ is a good fit between these two, as can be seen in figure 7. We use the elbow point since it provides a practical compromise between both points. This discrete $\text{AR}(7)$ model for residuals is consistent with an Ornstein–Uhlenbeck type mean-reverting process in continuous time; in particular, the AR coefficient ϕ provides an estimate of the daily persistence, from which we infer the mean-reversion speed $\kappa \approx -\ln(\sum_{i=1}^p \phi_i)$ for the temperature dynamics.

Euler Discretization for Temperature Simulation: To generate realistic temperature scenarios for derivative pricing, we developed a simulation algorithm based on the Euler discretization scheme. This approach combines our calibrated deterministic model with the stochastic AR process in a coherent framework. The simulation proceeds as follows:

1. For each time step t , we first calculate the deterministic component $\bar{\mu}(t)$ using our fitted sinusoidal model.

²See source code and documentation at: <https://github.com/open-meteo/open-meteo>

³See source code and documentation at: <https://scipy.org/>

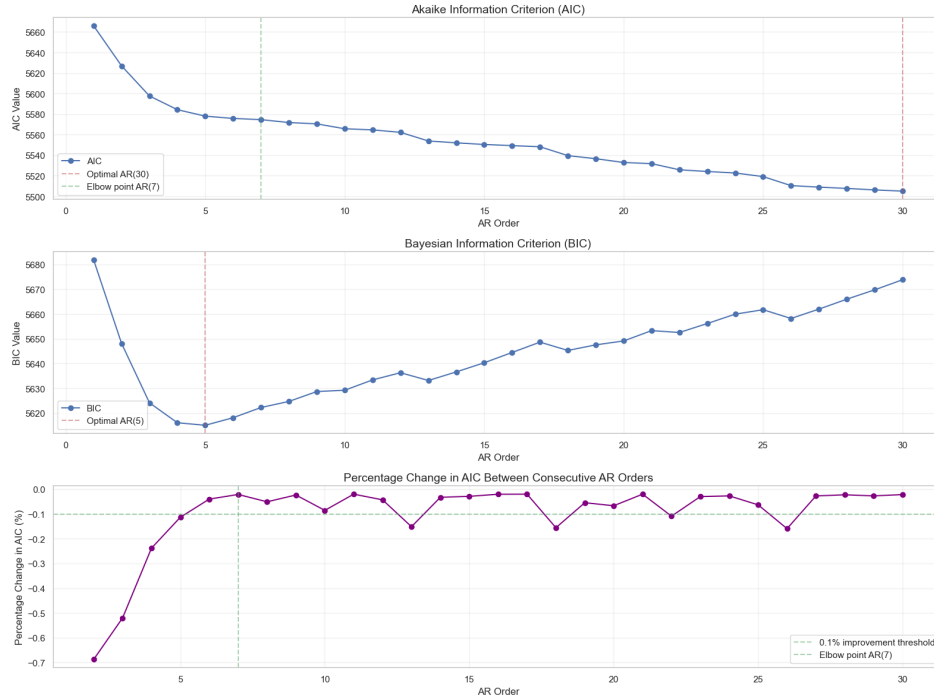


Figure 7: Graph of the change in values for AIC and BIC and the percentage change between the two. Important to note for AIC the optimal point will be even higher when plotted for even higher orders. However since we use the elbow point this doesn't affect our model.

2. We then simulate the stochastic residual r_t using the AR(7) process:

$$r_t = c + \sum_{i=1}^7 \phi_i r_{t-i} + \epsilon_t \quad (38)$$

where c is the constant term, ϕ_i are the AR coefficients, and $\epsilon_t \sim N(0, \sigma^2)$ represents random shocks.

3. The simulated temperature is then computed as $T_t = \bar{\mu}(t) + r_t$.

This approach preserves both the deterministic seasonal patterns and the stochastic day-to-day variations in temperature, while ensuring the mean-reverting property of temperature anomalies. To initialize the simulation, we use the most recent observed residuals as starting values, which allows for a smooth transition from historical to simulated data.

Weather Derivatives Pricing Framework: Building upon our temperature model, we implemented a comprehensive pricing framework for weather derivatives, focusing on three common contract structures: call options with caps, put options with floors, and collars. For each contract type, we define the payoff function in terms of cumulative degree days (DD) over the contract period.

A call option with cap pays

$$\xi = \min \{ \alpha \max(DD - K, 0), C \}, \quad (39)$$

where α is the notional amount per degree day, K is the strike level, and C is the maximum payout cap.

Similarly, a put option with floor pays

$$\xi = \min \{ \alpha \max(K - DD, 0), F \}, \quad (40)$$

where F represents the maximum payout floor.

A collar combines these structures, with payoff

$$\xi = \min \{ \alpha \max(DD - K_1, 0), C \} - \min \{ \beta \max(K_2 - DD, 0), F \}, \quad (41)$$

representing a long call position with a short put position.

To price these contracts, we employ Monte Carlo simulation using our calibrated temperature model. For each simulation path, we calculate the daily degree days—either Heating Degree Days (HDD) defined as $\max(18C - T_t, 0)$ (derived from equation (34)) or Cooling Degree Days (CDD) defined as $\max(T_t - 18C, 0)$ (derived from equation (35))—and aggregate them over the contract period to obtain the cumulative degree days. We then apply the appropriate payoff function and average across all simulation paths to estimate the expected payoff. The final price is obtained by applying a discount factor $e^{-r\tau}$, where r is the risk-free rate and τ is the time to maturity in years.

4.3 Results

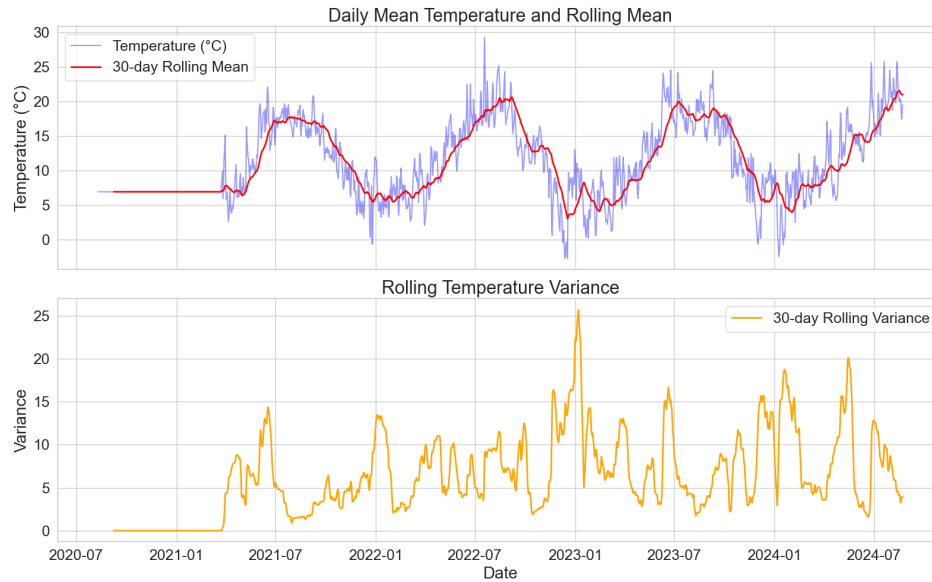


Figure 8: Daily mean temperature and rolling statistics. The top panel shows the observed daily mean temperature (blue) alongside a 30-day rolling mean (red). The bottom panel displays the corresponding 30-day rolling variance (orange).

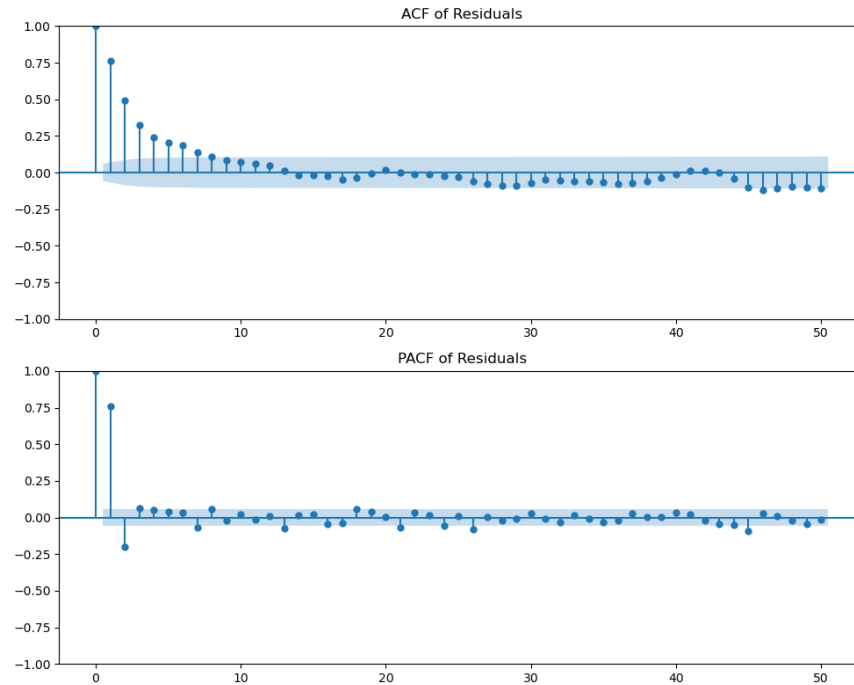


Figure 9: Autocorrelation and Partial Autocorrelation of Residuals. The top panel shows the autocorrelation function (ACF), and the bottom panel shows the partial autocorrelation function (PACF) of the residuals, each with 95% confidence intervals.

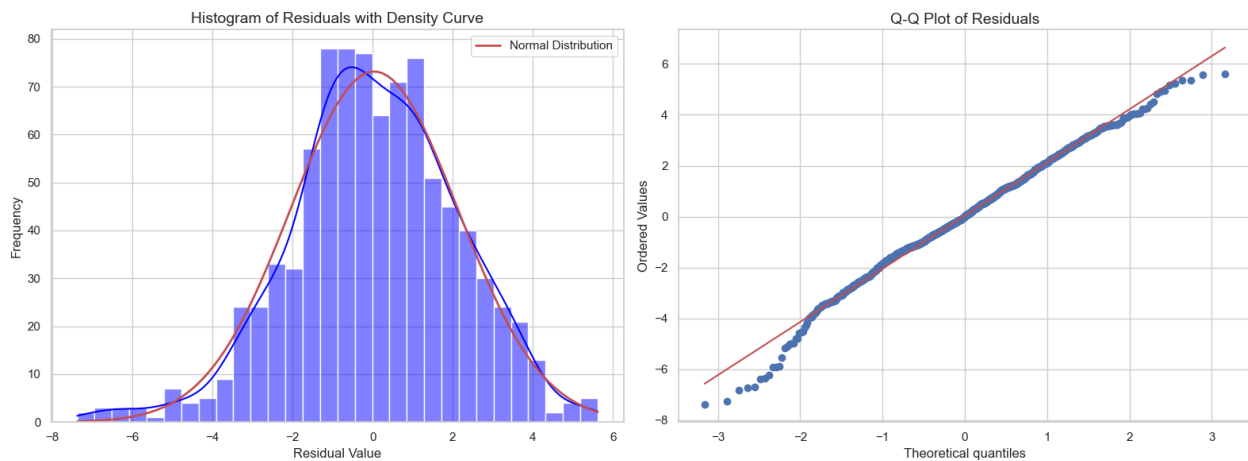


Figure 10: Distribution Analysis of Residuals. The left panel displays a histogram of the residuals overlaid with a kernel density estimate and a fitted normal distribution. The right panel shows a Q-Q plot comparing the quantiles of the residuals to a normal distribution.

4.4 Discussion

4.4.1 Data analysis

As an initial exploration of the dataset, we computed a 30-day rolling mean and rolling variance to examine the temporal structure of the temperature data. These are shown in Figure ???. The top panel displays the raw time series alongside its 30-day rolling average, which reveals a clear seasonal cycle suitable for modeling.

Parameter	Estimate
Baseline temperature (a)	9.2510 °C
Linear trend (b)	0.002625 °C/day (0.958955 °C/year)
Seasonal amplitude (α)	-6.1239 °C
Phase shift (θ)	-1.2732 rad (-72.95°)

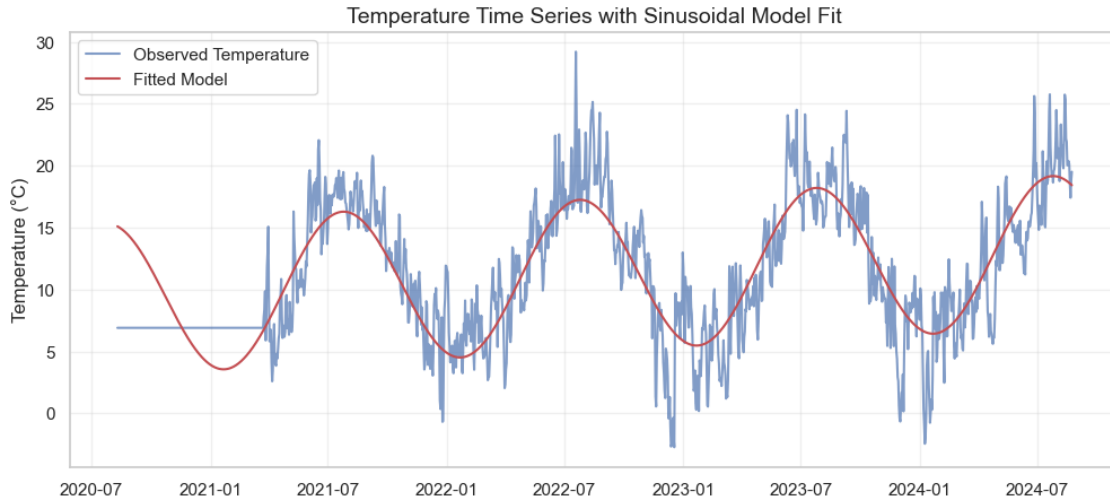
Table 5: Estimated parameters using `curve_fit` from the SciPy module.

Figure 11: Temperature time series with fitted sinusoidal model.

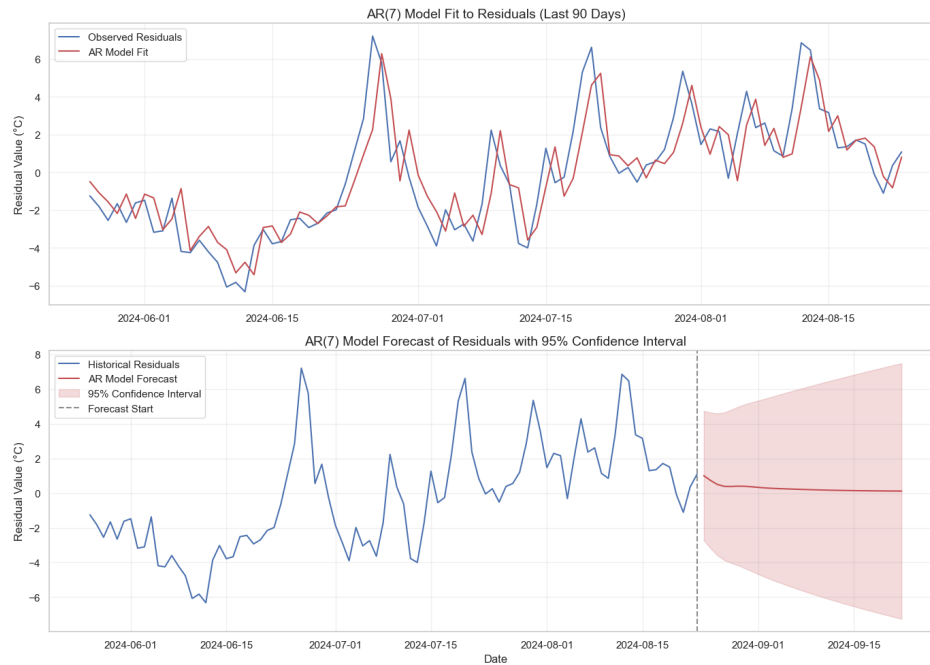


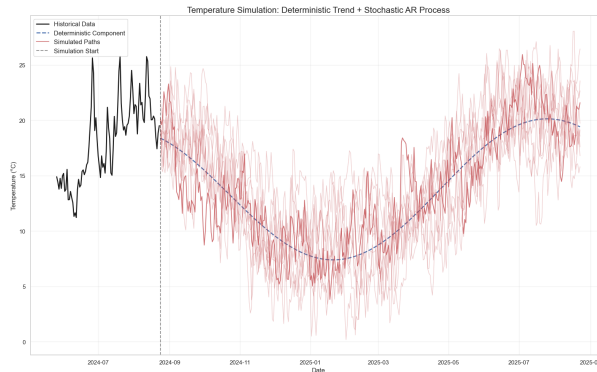
Figure 12: Temperature Time Series with AR(7) model.

Parameter	Estimate
Constant term a_0	2.2924
Harmonic 1 coefficient a_1	-0.0162
Harmonic 1 coefficient b_1	-0.1995
Harmonic 2 coefficient a_2	0.0770
Harmonic 2 coefficient b_2	0.1294

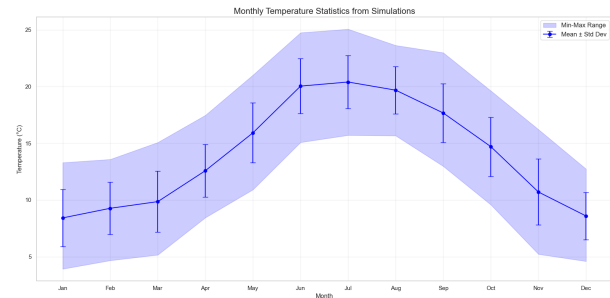
Table 6: Estimated Fourier coefficients for the seasonal volatility model.

AR Coefficients		Mean-Reversion Properties	
AR1	0.988	Sum of AR coefficients	0.872
AR2	-0.271	Mean-reversion parameter (κ)	0.137
AR3	0.058	Half-life (days)	5.04
AR4	0.038	Characteristic Roots (Moduli)	
AR5	0.032		
AR6	0.025		
AR7	0.002		
		Root 1	0.903
		Roots 2-3	0.635
		Roots 4-5	0.421
		Root 6	0.349
		Root 7	0.070

Table 7: AR(7) Model Results for Temperature Residuals.



(a) Sinusoidal signal with autoregression.



(b) Yearly trend sinusoidal signal with autoregression.

Figure 13: Results from sinusoidal signal with autoregression.

The bottom panel shows the corresponding rolling variance, where pronounced spikes indicate periods of increased temperature volatility. However, no consistent seasonal pattern is apparent solely in the variance itself.

To assess the residual distribution, we plotted a histogram and Q-Q plot (Figure 10). Both suggest that the residuals are approximately normally distributed, with the Q-Q plot showing close alignment to the reference line.

Figure 9 displays the autocorrelation (ACF) and partial autocorrelation (PACF) of the residuals. The ACF decays gradually, and the PACF shows a prominent spike at lag 1 before dropping off, consistent with a short-memory process. Most autocorrelations lie within the 95% confidence bounds, indicating the residuals resemble white noise—supporting the adequacy of the AR(7) model.

Contract Type	Parameters	Price (€)	Std Dev (€)	Max Payoff (€)	Min Payoff (€)
3*Call Option	Strike: 900 HDD	3*255.56	3*499.99	3*1,624.22	3*0.00
	Notional: €10/HDD				
	Cap: €5,000				
3*Put Option	Strike: 700 HDD	3*86.18	3*260.43	3*868.10	3*0.00
	Notional: €10/HDD				
	Floor: €3,000				
5*Collar	Call Strike: 800 HDD	5*670.92	5*853.21	5*2,624.22	5*0.00
	Put Strike: 600 HDD				
	Call Notional: €10/HDD				
	Put Notional: €8/HDD				
	Cap/Floor: €4,000/€2,000				
<i>Note:</i> Pricing based on 10 simulated temperature paths for Amsterdam from December 2024 to February 2025. Mean cumulative HDD: 832.81, Standard deviation: 123.74, Range: [613.19, 1062.42]. Discount rate: 3% per annum.					

Table 8: Weather Derivatives Pricing Results for Winter 2024-2025

Stationarity tests reinforce this conclusion. The Augmented Dickey-Fuller (ADF) test yields a statistic of -7.9355 ($p < 0.001$), and the KPSS test returns a statistic of 0.1172 ($p > 0.1$), together confirming that the residuals are stationary. This validates the effectiveness of our seasonal decomposition in removing trend and seasonality.

For the original temperature series, the ADF test (-2.2926 , $p = 0.1744$) indicates non-stationarity, while the KPSS test (0.1656 , $p > 0.1$) suggests trend-stationarity. This common discrepancy highlights the presence of deterministic seasonal patterns—exactly what our sinusoidal seasonal model aims to capture.

4.4.2 Model analysis

Sinusoidal Model: First we fitted the sinusoidal Model, this can be seen in figure 11. On first look the model seems to be fitted really well and seems to, when the measurements start happening, follow the trend really well. The statistics also show this. The residuals show a mean of 0.0000 , which indicate the model is unbiased. Also both the ADF p-value of 0.000 and the KPSS of 0.100 strongly indicate that the residuals are stationary. The standard deviation of the model seems quite high with 3.1786°C , which show that the model tracks the general trend really well, but does badly at predicting specific moments.

Autoregressive model and Seasonal Volatility: The upper plot in figure 12 shows the AR(7) model fitting the residuals closely, indicating a strong match between model and data.

Table 7 summarizes key features of the AR(7) model. The dominant first-order coefficient (0.988) reflects high day-to-day persistence, while the negative second-order coefficient (0.271) introduces a stabilizing correction that prevents prolonged anomalies. The mean-reversion rate ($\kappa = 0.137$) implies a half-life of roughly 5 days, which is consistent with typical meteorological variability.

All characteristic roots lie within the unit circle, confirming stationarity. Some roots are complex, indicating oscillatory rather than purely decaying behavior in the residuals.

These results complement the deterministic seasonal model by capturing short-term stochastic fluctuations in temperature. Together, they form a robust representation of both predictable seasonal patterns and unpredictable weather-driven variations.

The forecast on the bottom plot in figure 12 seems weird at first sight, as you would assume the oscillations to continue. However since we are looking at residuals we would also expect mean reversion (which is a gradual return towards zero), and is exactly what we observe. We additionally expect some oscillations in the prediction, and we do see this but these are only very small in figure 12. This is likely because the final

measure of the residuals is already relatively close to 0. What we also see is that for the prediction there is a very high confidence interval which is growing as time goes on. This is explained by the high variability in the temperature data.

Seasonal Volatility Modeling: Further enhancing our model, we implemented a seasonal volatility component using Fourier series with two harmonics. The Fourier parameters (constant term $a_0 = 2.2924$, first harmonic coefficients $a_1 = -0.0162$ and $b_1 = -0.1995$, and second harmonic coefficients $a_2 = 0.0770$ and $b_2 = 0.1294$) capture the seasonal pattern in temperature variability, as can be seen in table 6.

The negative b_1 coefficient indicates that volatility tends to decrease during the spring and increase during the fall, which aligns with meteorological observations that temperature variability is typically higher during seasonal transitions. The positive a_2 and b_2 coefficients introduce a secondary oscillation that refines this pattern, capturing more nuanced seasonal effects.

This seasonal volatility modeling is particularly important for weather derivatives pricing, as it accounts for the heteroskedasticity in temperature data—the fact that temperature variability itself varies throughout the year. Traditional constant-volatility models would underestimate risk during high-volatility periods and overestimate it during low-volatility periods, potentially leading to mispricing of weather derivatives.

The residual standard deviation of 1.6058°C represents the baseline volatility, which is then modulated by the seasonal pattern. This approach provides a more realistic representation of temperature dynamics than assuming constant volatility throughout the year, especially for longer-term contracts that span multiple seasons.

Integrated Model Assessment: The combined deterministic trend (with parameters $a = 9.2510$, $b = 0.002625$ $^\circ\text{C}/\text{day}$, $\alpha = -6.1239$, and $\theta = -1.2732$ radians), AR(7) stochastic component, and seasonal volatility creates a comprehensive temperature model that captures:

1. Long-term climate trends (through the linear component b).
2. Seasonal patterns (through the sinusoidal component).
3. Short-term persistence and mean-reversion (through the AR coefficients).
4. Seasonal variations in volatility (through the Fourier volatility model).

The small positive trend coefficient seen in Table 5 ($b = 0.002625$ $^\circ\text{C}/\text{day}$, equivalent to approximately 0.96°C per year) aligns with observed warming trends in Amsterdam's climate. The mean-reversion parameter ($\kappa = 0.137$) confirms that temperature anomalies tend to dissipate within about a week, providing useful information for short-term derivative contracts.

Euler Discretization for Temperature Simulation: In figure 13 we see the combination of both the AR model and the sinusoidal model. In figure 13a We first see the histrocal data followed by the start of the simulation. We see multiple simulations all generally following the general sinusiodial trend, with some deviations for the different simulations. This is what we would expect as the process is uncertain. In figure 13b we see the general trend for the year. We see for example that during June, July, August the temperature is general higher then during months such as January and February.

Weather Derivatives Pricing: As can be seen in table 8 our weather derivatives pricing framework yielded insightful results for the winter period (December 2024 to February 2025). The simulated temperature paths produced a mean of 832.81 cumulative HDDs with a standard deviation of 123.74, reflecting the inherent

variability in winter temperatures. This variability is crucial for understanding the risk profile of weather derivatives.

The call option with a strike of 900 HDDs and €10 per degree day notional was priced at €255.56, representing the expected value of winter temperatures exceeding the strike. This relatively modest price reflects that the strike is above the mean HDD (832.81), making the option out-of-the-money on average. However, the substantial standard deviation of payoffs (€499.99) highlights the significant upside potential, with maximum payouts reaching €1,624.22 in severe winter scenarios.

Conversely, the put option with a strike of 700 HDDs was priced at €86.18, offering protection against milder-than-expected winters. The lower price compared to the call option is consistent with the put being further out-of-the-money relative to the mean HDD. The collar structure, combining a long call (strike 800) with a short put (strike 600), was priced at €670.92, providing a cost-effective way to hedge against temperature extremes while partially offsetting the premium through the short put position.

These pricing results demonstrate how our temperature model can be applied to quantify weather risk in financial terms. The substantial variability in potential payoffs underscores the importance of accurate temperature modeling for weather risk management. The mean-reverting properties captured by our AR(7) model are particularly relevant for these derivatives, as they directly influence the probability distribution of cumulative degree days and, consequently, the option prices.

The pricing framework also reveals the asymmetric nature of temperature risk in Amsterdam winters. The higher call option price relative to the put (despite both being similarly out-of-the-money) suggests that the market would place a premium on protection against unexpectedly cold winters, consistent with the positive skew observed in our simulated HDD distribution. This asymmetry is valuable information for entities with temperature-sensitive operations or costs.

Furthermore, the collar's price structure illustrates how combined positions can create customized risk profiles, allowing market participants to efficiently hedge specific temperature exposures. The significant maximum payoff (€2,624.22) demonstrates the potential value of these instruments during extreme weather events, precisely when financial protection is most needed.

4.5 Conclusion

In this project, we built a model to simulate daily temperatures in Amsterdam and used it to price weather derivatives based on Heating Degree Days (HDD). By combining a sinusoidal trend model with an AR(7) process for short-term fluctuations and adding a seasonal volatility component, we were able to capture both the predictable patterns and the day-to-day randomness in temperature data. Our statistical checks confirmed that the model fits the data well and reflects key features like mean reversion and changing volatility throughout the year. Using this model, we ran Monte Carlo simulations to estimate the value of various HDD-based weather contracts. The results showed clear differences in payoff depending on the contract structure, strike levels, and temperature variability. Even contracts that looked unlikely to pay off on average still carried significant potential value in extreme scenarios. Overall, this work shows how a solid temperature model can be used to make informed decisions regarding weather risk.

5 Conclusion

This report has demonstrated how computational finance balances analytic tractability with simulation-based methods to price a variety of derivatives.

Beginning with variance swaps, we showed that realised variance admits a closed-form replication using log-contracts and dynamic hedging, yielding an exact expression for the fair variance strike under the Heston model. This analytic approach underscores the power of no-arbitrage arguments when markets are complete and payoffs can be decomposed into standard instruments.

By contrast, pricing an arithmetic Asian option under stochastic volatility requires Monte Carlo simulation, since no closed-form solution exists. Here, we implemented both Euler and Milstein discretizations of the Heston model and introduced a control variate—namely, the known price of a geometric Asian option—to dramatically reduce estimator variance. This variance-reduction technique cut the simulation cost by an order of magnitude, illustrating that even complex path-dependent payoffs become tractable when enhanced by clever statistical methods.

Finally, in the context of temperature derivatives, we developed a bespoke seasonal–mean–reverting model for daily Amsterdam temperatures. After fitting a sinusoidal trend and an AR(7) residual process to historical data, we generated temperature paths via Euler discretization. Lacking any replication framework in an incomplete market, we relied entirely on Monte Carlo to estimate payoffs on heating- and cooling-degree-day contracts. This section highlights the flexibility of simulation methods to handle non-financial underlyings and emphasizes the importance of careful model calibration.

Across all three case studies, the unifying principle has been expectation under an appropriate measure—computed analytically when possible and via Monte Carlo otherwise. Whenever simulation was necessary, variance reduction proved essential to achieve reliable results without excessive computational effort. Moreover, each application required tailored calibration: from option-implied volatility surfaces to statistical fits of meteorological time series. Together, these examples illustrate a coherent workflow for modern derivative pricing: identify whether analytic solutions exist; if not, choose and implement efficient simulation techniques; and always validate models against data.

References

- Boyle, P. P. (1977). Options: A monte carlo approach. *Journal of financial economics*, 4(3), 323–338.
- Hull, J., & White, A. (1988). The use of the control variate technique in option pricing. *Journal of Financial and Quantitative analysis*, 23(3), 237–251.